

LLM-driven discovery for carbon allotropes with bond-network entropy

Yuzhou Hao,¹ Yujie Liu,¹ Xuejie Li,¹ Turab Lookman,² Xiangdong Ding,¹ Jun Sun,¹ and Zhibin Gao^{1,†}

¹State Key Laboratory for Mechanical Behavior of Materials,

State Key Laboratory of Porous Metal Materials,

School of Materials Science and Engineering, Xi'an Jiaotong University, Xi'an 710049, China

²AiMaterials Research LLC, Santa Fe, New Mexico 87501, USA

(Dated: February 27, 2026)

The discovery of novel carbon allotropes with tailored thermal and mechanical properties is critical for advanced thermal management. However, exploring the vast configurational space of carbon using *ab initio* calculations remains computationally prohibitive. Driven by the rich topological landscape of carbon, where the competition between sp , sp^2 , and sp^3 hybridization states dictates material performance, we establish a closed-loop AI framework to explore this complex configurational space. We introduce a hybridization entropy descriptor to guide the search beyond conventional forms. Here, we establish a closed-loop AI framework that synergizes a Large Language Model (LLM) for structural generation with a Machine Learning Potential (MLP) for accelerated evaluation. Leveraging CrystaLLM to generate candidates and an iteratively refined MLP for high-fidelity validation, we screened thousands of structures to identify several stable allotropes with exotic properties. Specifically, we report “yne-diamond C₁₂” and “yne-hex-diamond C₈”, which exhibit extreme thermal anisotropy and ultralow in-plane shear stiffness arising from their mixed sp - sp^3 hybridization. Furthermore, we discovered a complex sp - sp^2 - sp^3 hybridized C₁₂ phase that combines metallic conductivity with an anomalous negative Poisson’s ratio. Notably, we identified a superhard phase (C16.3) possessing a calculated Vickers hardness (103.3 GPa) exceeding that of diamond 96 GPa [1]. Microscopic analysis reveals that thermal transport in these materials is governed by the interplay between rigid frameworks and flexible linkers. This work expands the known carbon phase space and demonstrates the efficacy of coupling generative AI with machine learning potentials for the accelerated inverse design of functional materials.

Carbon materials, ranging from 3D diamond to 2D graphene and 1D carbon nanotubes [2–4], are critical to thermal management, electronics, and energy storage owing to their unique sp , sp^2 , and sp^3 hybridization-induced properties [5]. Despite this rich polymorphic landscape, discovering new thermodynamically stable allotropes with tailored properties (e.g., high thermal conductivity, hardness or mechanical anisotropy) remains challenging. Conventional approaches, including random structure searching and evolutionary algorithms such as USPEX [6] and CALYPSO [7], are often constrained by low search efficiency and the high computational cost of first principle calculations.

Artificial intelligence (AI) has emerged as a transformative tool in materials science. Beyond earlier generative models like Graph Neural Networks (GNNs) and Variational Autoencoders (VAEs) [8, 9], Large Language Models (LLMs) such as CrystaLLM [10, 11] have shown that treating crystallographic data as text sequences enables the generation of chemically valid structures. The scalability of such approaches was further demonstrated by the Graph Networks for Materials Exploration (GNoME) [12]. However, a critical challenge persists: coupling LLM-based generation with a rapid, high-fidelity validation framework that can handle complex, non-equilibrium bonding environments without incurring the prohibitive computational burden of *ab initio* calculations.

To address this, we propose a comprehensive dual-

loop active learning (AL) framework, shown in Fig. 1. The first loop leverages an LLM to explore the carbon compositional space, generating candidate structures containing up to 100 atoms per conventional cell (C1–C100, optimized by MatterSim [13]). These candidates are rapidly screened: first by our homegrown PINK code [14] for preliminary lattice thermal conductivity (κ_L) estimation, and subsequently for dynamical stability using Phonopy [15] combined with the current iteration of our Machine Learning Potential (MLP). The second loop supports this generation by iteratively constructing a universal MLP, based on the Neuroevolution Potential (NEP) architecture [16]. Unlike standard empirical potentials, this MLP is actively retrained by sampling diverse, extreme configurations—ranging from ultra-high pressure phases (> 500 GPa, shown in Fig. 3(c) and strain stress relationship in Fig. S5) to complex mixed-hybridization networks—thereby ensuring DFT-level accuracy across the entire potential energy surface. This workflow seamlessly connects generative design with high-fidelity physical property calculations (using GPUMD [17], LAMMPS [18], and CSLD [19]), culminating in the accelerated discovery of novel carbon materials with customized mechanical and thermal properties.

Here, we employ this framework to explore the configuration space of carbon, identifying stable allotropes that include high-density superhard phases and porous anisotropic frameworks. Crucially, our search is driven

arXiv:2602.22706v1 [cond-mat.mtrl-sci] 26 Feb 2026

by a specific physical motivation: to overcome the limitations of pure sp^3 networks (which are thermally isotropic and brittle) by exploring the ‘mixed-hybridization’ topological space. We hypothesize that introducing sp -hybridized acetylenic linkers or sp^2 nodes into a rigid sp^3 framework can decouple thermal transport from mechanical stiffness. This ‘phonon engineering’ strategy aims to identify metastable phases where the interplay between rigid frameworks and flexible linkers enables exotic functionalities. We focus on three exemplary structures: yne-diamond C_{12} , yne-hex-diamond C_8 , and a complex sp - sp^2 - sp^3 hybrid C_{12} [20–23]. Combining the Boltzmann Transport Equation (BTE) with heterogeneous non-equilibrium molecular dynamics (HNEMD) [24], we elucidate the microscopic mechanisms governing thermal transport in these systems. These results demonstrate the critical role of AI-assisted design in discovering materials with extreme properties beyond the reach of traditional screening methods.

The NEP training dataset covers a comprehensive range of structural configurations and stress states. As shown in Fig. 2(a), the loss functions exhibit excellent convergence: over 2×10^5 steps, the root-mean-square error (RMSE) for energy and force decreases to 0.16 eV/atom and 0.65 eV/Å, respectively, with the virial RMSE reaching 0.40 eV/atom. These trends suggest that sufficient accuracy for phonon calculations is achieved beyond 10^5 steps. Additionally, stable L_1 and L_2 regularization curves indicate effective complexity control, ensuring model transferability across different sp -hybridized structures without overfitting.

Fig. 2(b) illustrates the atomic environment distribution within the descriptor space, with Descriptors A and B ranging from -0.1 to 0.4 and -0.2 to 0.8, respectively. Data points are color-mapped by energy [-7.0 eV/atom (dark blue) to -1.0 eV/atom (pink)], with marker sizes scaled to represent the energy fitting error. This extensive coverage verifies the training set’s capability to represent a wide spectrum of bonding and stress configurations [25].

Fig. 2(c) displays representative fullerene derivatives (c_1 - c_5), ranging from isolated C_{60} to 1D C_{70} chains and monolayer fullerene networks (c_3). Layered graphene configurations (d_1 - d_3) with distinct stacking sequences and vacancy defects are shown in Fig. 2(d), providing insight into anisotropic thermal transport. Fig. 2(e) highlights diamond polytypes (e_1 - e_3), specifically comparing hcp-diamond (e_1) and fcc-diamond (e_3) phases. Furthermore, Fig. 2(f) presents sp -hybridized allotropes (f_1 - f_8), such as carbyne (f_1) and graphdiyne (f_8), which have gained prominence for their exceptional properties since their theoretical prediction [26, 27].

Fig. 2(g) further illustrates complex 3D network structures (g_1 - g_9). By encompassing the full range of hybridization states (sp , sp^2 , sp^3) and dimensionalities (1D–3D), the dataset ensures the NEP’s applicability

to diverse carbon materials for thermal and mechanical properties. Crucially, the active learning workflow systematically targets high-uncertainty structural configurations, thereby optimizing the training efficiency.

To evaluate the transferability of the carbon NEP, we validate it against an independent test set containing diamond (sp^3), graphene (sp^2), and carbyne (sp). As shown in Fig. 3(a), the allotropes form distinct clusters in the descriptor space: diamond (purple), graphene (blue), and carbyne (red). This separation demonstrates the model’s ability to discriminate between local environments characteristic of different hybridization states. In the plot, color denotes atomic energy, and marker size corresponds to the prediction error relative to density functional theory (DFT) data. Fig. 3(b-d) compare NEP predictions against DFT benchmarks calculated using the optB86b functional (to account for van der Waals interactions). Fig. 3(b) highlights the energy accuracy, showing exceptional linearity over a wide energy window. The model achieves high fidelity in both low-energy equilibrium states and high-energy distorted configurations, a prerequisite for robust thermodynamic stability analysis.

The robustness of the potential under extreme mechanical conditions is further evidenced by the virial stress and atomic force predictions. Fig. 3(c) shows that the predicted virial stresses align with DFT data over a remarkably broad range, from tensile states of -400 GPa to compression exceeding 1000 GPa. This dynamic range, rarely achieved by empirical potentials, ensures the description of severe strain without non-physical artifacts. Similarly, Fig. 3(d) demonstrates high accuracy in atomic force predictions up to 150 eV/Å. Capturing such extreme forces and stresses is critical for ensuring MD simulation stability, enabling the reliable exploration of phase transitions and mechanical properties under extreme pressures.

We calculated phonon dispersion relations for six representative carbon allotropes (Fig. 4(a-f)) to verify the NEP’s capability in capturing lattice dynamics across distinct dimensionalities and hybridization. As rigorous benchmarks, Figs. 4(a-c) show the phonon spectra for ideal sp^3 networks (cubic and hexagonal diamond [28, 29]) and the archetypal 2D sp^2 system (graphene). To further test transferability to metastable phases relevant to high-pressure synthesis and generative design, we analyzed the body-centered cubic BC8 phase (Fig. 4(d)) [30–33], the monolayer quasi-hexagonal fullerene network (Fig. 4(e)) [34–37], and the body-centered tetragonal C4 allotrope (Fig. 4(f)) [38, 39].

The NEP predictions (dashed blue lines) show remarkable agreement with DFT benchmarks (solid red lines) throughout the Brillouin zone. The acoustic branches, critical for thermal transport, are reproduced with high fidelity, especially near the Γ point (determining group velocities). Similarly, the excellent alignment of optical modes confirms the accurate description of C-C bond

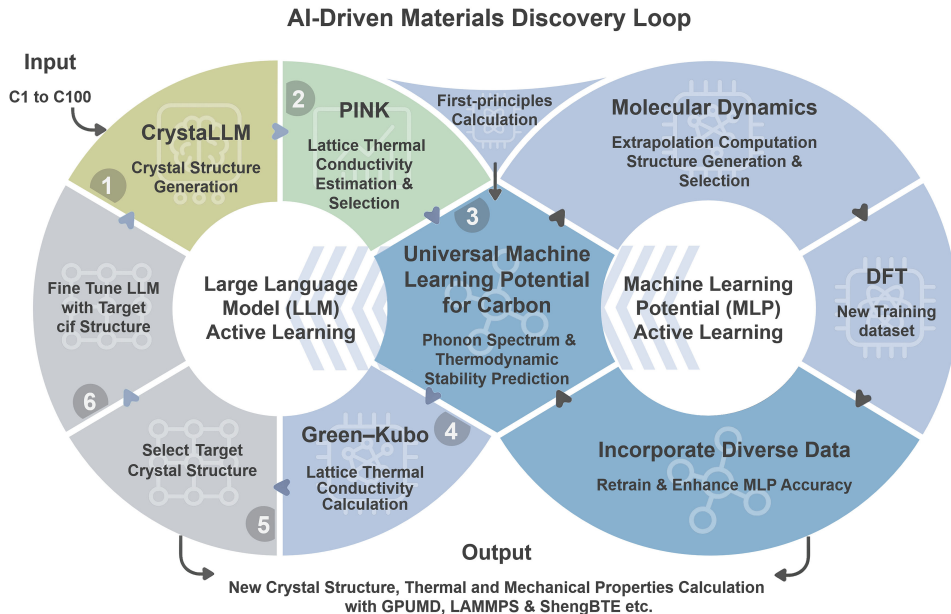


FIG. 1. Schematic illustration of the closed-loop AI-driven materials discovery workflow. The framework integrates two synergistic active-learning cycles. The generative cycle (left) utilizes a Large Language Model (CrystaLLM) to propose and screen candidate structures with varying atom counts (C1–C100), followed by fine-tuning on DFT-verified stable phases. The potential training cycle (right) iteratively refines the Machine Learning Potential (MLP) using on-the-fly data generation. This combined pipeline enables rapid high-throughput screening and accurate thermal/mechanical property evaluation via GPUMD and ShengBTE simulations.

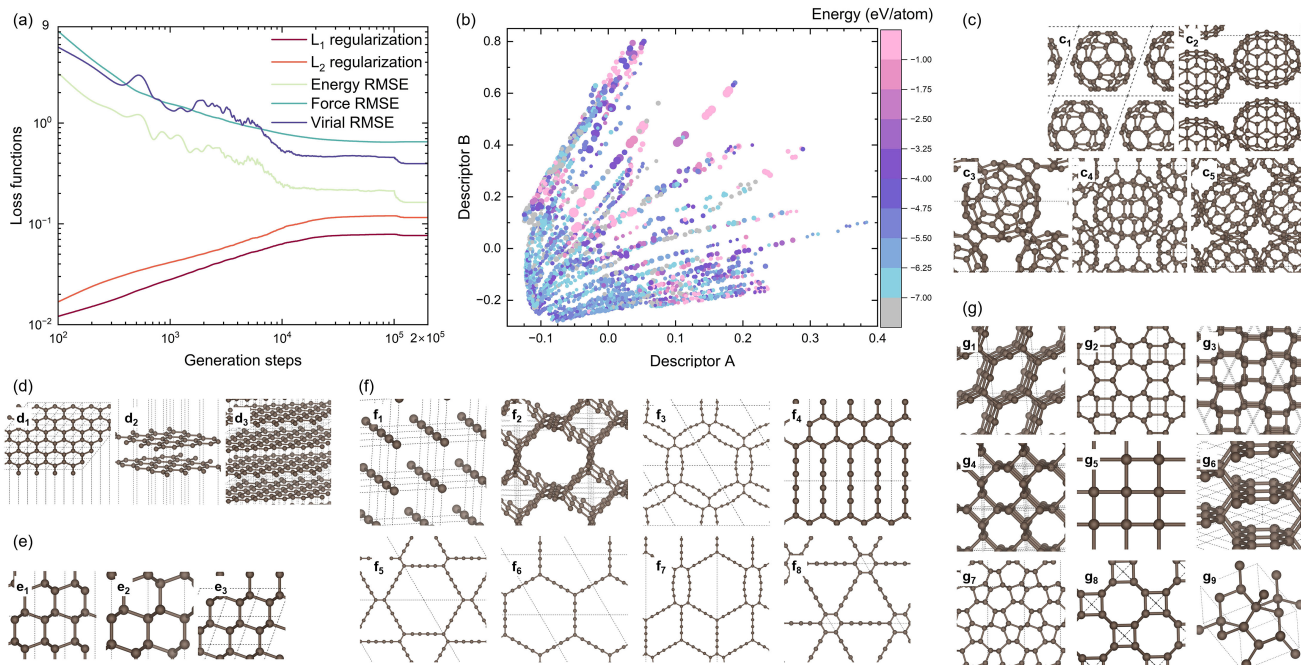


FIG. 2. Training performance and dataset diversity of the carbon Machine Learning Potential (NEP). (a) Evolution of loss functions (including L_1/L_2 regularization) and RMSE values for energy, force, and virial versus training steps, illustrating model convergence. (b) Distribution of atomic environments in the descriptor space, color-coded by energy per atom, demonstrating comprehensive structural coverage. (c)–(g) Representative structures from the training set, including fullerenes (c_1 – c_6), layered graphene (d_1 – d_3), diamond (e_1 – e_3), sp hybridization states carbon (f_1 – f_8) and diverse 3D frameworks (g_1 – g_9).

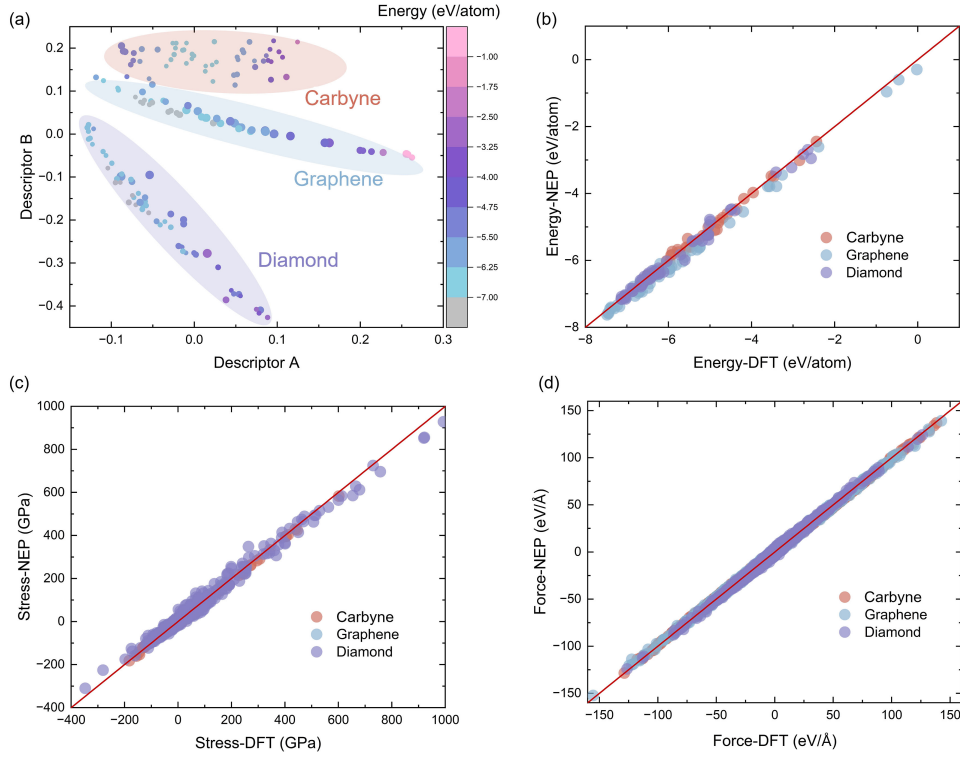


FIG. 3. Validation of the NEP model against DFT benchmarks. (a) Visualization of atomic environments in the descriptor space, showing distinct clustering for carbyne (red), graphene (light blue), and diamond (dark blue). (b)–(d) Parity plots comparing NEP predictions with DFT calculations for (b) energy per atom, (c) virial stress, and (d) atomic forces. The diagonal lines indicate perfect agreement.

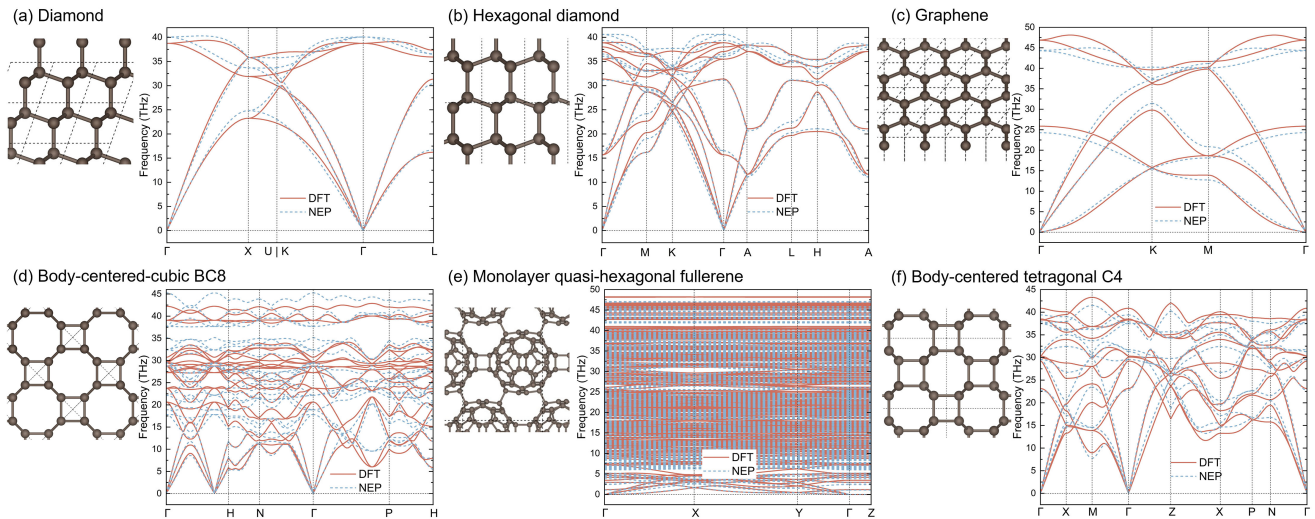


FIG. 4. Phonon dispersion relations for representative carbon allotropes. Comparison between predictions from the NEP model (dashed blue lines) and DFT benchmarks (solid red lines). The panels show: (a) cubic diamond, (b) hexagonal diamond, (c) monolayer graphene, (d) body-centered cubic BC8, (e) monolayer quasi-hexagonal fullerene, and (f) body-centered tetragonal C₄.

stiffness across varying sp^2 and sp^3 environments. Finally, the absence of imaginary modes in all calculations verifies that the NEP correctly identifies these diverse allotropes as dynamically stable energy minima.

Given the model’s accuracy in the harmonic regime, we further, using the homogeneous non-equilibrium molecular dynamics (HNEMD) method, validate its prediction of lattice thermal conductivity (κ_L) which is very sensitive to anharmonic scattering. As summarized in Table S1 (Supplementary Material), the NEP correctly reproduces the established thermal transport hierarchy. Specifically, compared to the high- κ_L diamond and graphene, the complex metastable phases (BC8, C4, and quasi-hexagonal fullerene) exhibit significantly reduced κ_L due to enhanced phonon scattering arising from lower symmetry and complex crystal structures. This quantitative consistency confirms the NEP’s reliability for high-throughput thermal and mechanical property screening.

Utilizing the AI-driven workflow, we screened thousands of CrystaLLM-generated candidates to isolate dynamically stable carbon allotropes. Fig. 5 displays six representative phases (e.g., C52_15, denoting the 15th candidate with a target size of 52 atoms/cell) alongside their NEP-calculated phonon spectra. Crucially, all six structures exhibit real frequencies throughout the Brillouin zone, confirming their status as dynamically stable local minima on the potential energy surface. This high hit rate underscores the efficacy of our active learning strategy. Detailed statistics on candidates discarded due to thermodynamic or dynamic instability are provided in the Supplementary Material to demonstrate the rigor of the filtering process.

These allotropes display a broad spectrum of topologies, spanning open frameworks to dense networks, which drives their distinct physical behaviors. A prime example is C22_6 (Fig. 5(c)), distinguished by its porous, ring-based architecture. This structural anisotropy engenders highly directional chemical bonding and, consequently, extreme anisotropy in lattice thermal conductivity, offering significant potential for directional heat channeling. In contrast, the C16_3 phase (Fig. 5(e)) features a dense sp^3 -dominant network, yielding a potential superhard material. Its calculated hardness reaches 103.3 GPa calculated via the Chen model [40], exceeding the value for diamond obtained in this framework (91.8 GPa) as well as previous theoretical 93.6 GPa [41] and experimental 96 GPa [1]). In addition, structures like C24_4 (Fig. 5(b)) and C52_15 (Fig. 5(f)) exhibit complex lattices with mixed hybridization, providing a tunable trade-off between porosity and mechanical stability.

We further evaluated the mechanical and thermal performance of the discovered phases. As summarized in Table S1, we computed κ_L , density, and Vickers hardness (calculated via the Chen model [40]: $H_v = 2(k^2G)^{0.585} - 3$). The results span a broad spectrum of κ_L values, gov-

erned by the specific structural complexity and lattice anisotropy of each allotrope. The successful identification of extreme phases—specifically the superhard C16_3 and the highly anisotropic C22_6 demonstrates the generative model’s unique ability to navigate “hidden” regions of the structural landscape, surpassing the limitations of conventional heuristic searches.

Among the discovered phases, three standout structures exhibit unique mixed-hybridization topologies (Fig. 6). We term the first two “yne-diamond C_{12} ” (Fig. 6(a)) and “yne-hex-diamond C_8 ” (Fig. 6(c)) [20–22]. Analogous to graphdiyne, these structures are conceptually formed by inserting linear sp -chains (acetylenic linkages) into the C-C bonds of cubic and hexagonal diamond, respectively. The hybridization hierarchy is visualized in Fig. 6 (blue: sp^3 , yellow: sp , orange: sp^2). Furthermore, the charge density maps (Fig. 6(b, d)) show strong electron localization along the bond axes, indicative of insulating or semiconducting behavior.

The third structure, an sp - sp^2 - sp^3 hybridized C_{12} (Figs. 6(e, f)), features a complex ternary hybridization containing all three carbon coordination states [23]. Its architecture displays a unique layered motif: rigid sp^3 frameworks bridged by sp - sp^2 networks. Crucially, the charge density map (Fig. 6(g)) indicates significant electron delocalization along these sp - sp^2 linkages, pointing to a metallic nature. This is corroborated by subsequent band structure calculations (Fig. 7), which classify this C_{12} phase as an electrical conductor, distinct from the insulating behavior typical of pure sp^3 networks.

To comprehensively assess the performance potential of these three allotropes, we calculated their mechanical and thermal properties, as summarized in Table S1 (Supplementary Material). The data highlight remarkable mechanical anisotropy. Specifically, while these structures maintain a high Young’s modulus along the covalent backbone (indicating high axial stiffness), they exhibit an ultralow in-plane shear modulus that is a feature often associated with lubricity or flexibility in specific directions. Most notably, the sp - sp^2 - sp^3 hybridized structure exhibits a negative Poisson’s ratio. This rare auxetic behavior, where the material expands laterally under tension, is highly unusual for carbon networks [23, 42]. However, it is important to note that this specific structure approaches the limit of dynamical stability. Phonon calculations reveal soft imaginary phonon modes near the Γ point, and *ab initio* molecular dynamics (AIMD) simulations suggest dynamical stability is maintained only up to approximately 100 K. Despite this low-temperature limitation, the unique coexistence of metallic conductivity and auxeticity offers valuable insights into the design rules for exotic carbon functional materials.

To rigorously verify prediction reliability and elucidate the electronic nature of these discovered materials, we calculated their phonon dispersion relations and electronic band structures, as presented in Fig. 7.

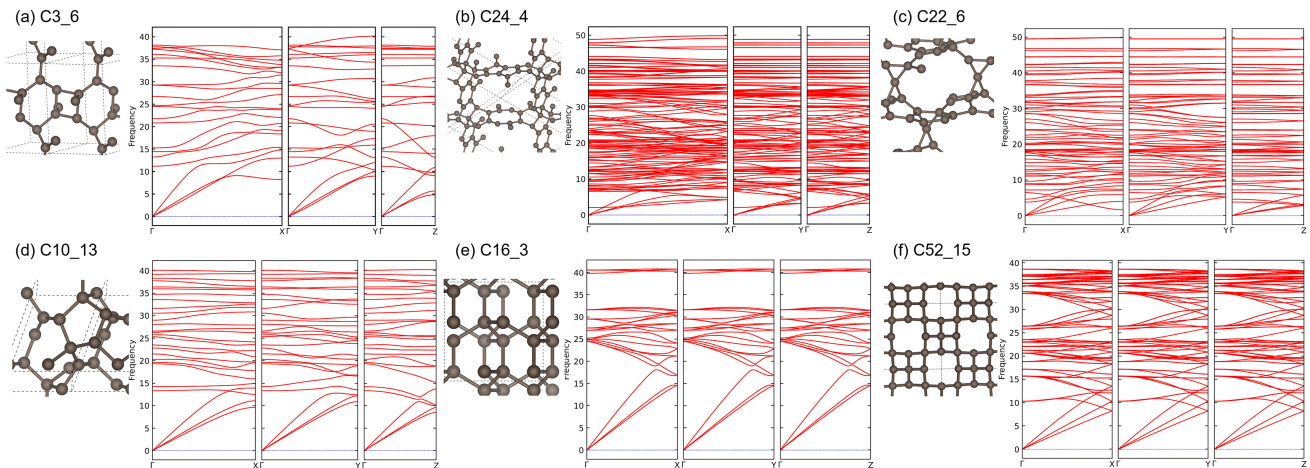


FIG. 5. Newly discovered stable carbon allotropes and their phonon spectra. (a)–(f) Representative structures generated by the LLM alongside their phonon dispersion relations calculated by the NEP. The structures are labeled as: (a) C3_6, (b) C24_4, (c) C22_6, (d) C10_13, (e) C16_3, and (f) C52_15. Here, the notation C_{n_m} denotes the m -th predicted candidate from a generative prompt for n atoms in the conventional cell. The absence of imaginary frequencies confirms the dynamical stability of all shown phases.

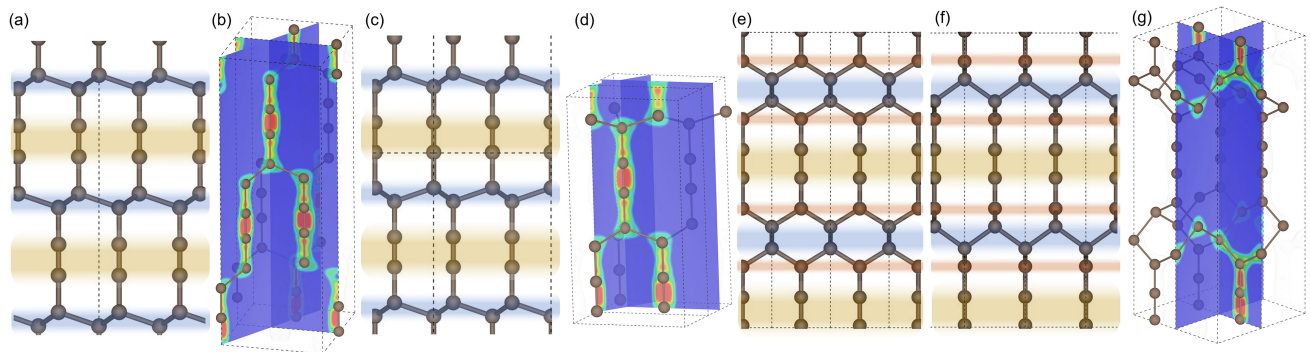


FIG. 6. Structural and charge density distributions of standout allotropes. (a, b) yne-diamond C_{12} ; (c, d) yne-hex-diamond C_8 ; and (e–g) the sp - sp^2 - sp^3 hybridized C_{12} [(e) front view, (f) side view, (g) charge density]. In the structural models, atoms are color-coded by hybridization: sp^3 (blue), sp^2 (orange), and sp (yellow). The corresponding charge density maps [(b), (d), (g)] illustrate electron distribution, with red/yellow isosurfaces indicating accumulation and blue regions indicating depletion.

Figs. 7(a–c) display the phonon spectra for yne-diamond C_{12} , yne-hex-diamond C_8 , and the sp - sp^2 - sp^3 hybrid C_{12} , respectively. To explicitly demonstrate the efficacy of the active learning strategy (see Fig. 1), we compare the results from two generations of the potential: the initial universal potential (NEP1, dashed light blue lines) and the final, iteratively refined potential (NEP2, dashed purple lines), plotted alongside the benchmark DFT data (solid red lines). Although NEP1 reproduces the dispersion, it deviates significantly in the high-frequency optical branches governing bond stretching. Conversely, the refined NEP2 achieves near-perfect agreement with DFT throughout the frequency spectrum. This enhancement underscores the efficacy of the active learning strategy in identifying and learning from high-uncertainty configurations. Consequently, the first two structures show no imaginary modes, confirming dynamical stability. For the third phase (Fig. 7(c)), soft modes near Γ indicate

lattice flexibility, consistent with the metastability observed in AIMD.

In addition to stability, these allotropes offer tunable electronic properties. Using the HSE06 hybrid functional for accurate bandgap assessment, we find that yne-diamond C_{12} (Fig. 7(d)) and yne-hex-diamond C_8 (Fig. 7(e)) are indirect semiconductors with narrow bandgaps of 0.64 eV and 0.25 eV, respectively, which are ideal for infrared or thermoelectric applications. Conversely, the sp - sp^2 - sp^3 hybrid (Fig. 7(f)) is metallic, with bands crossing the Fermi level. As indicated by the charge density (Fig. 6), this conductivity arises from π -electron delocalization in the sp - sp^2 network. This demonstration of tuning carbon from a wide-bandgap insulator to semiconductors and metals via hybridization topology underscores the power of our generative framework.

To elucidate the microscopic thermal transport mech-

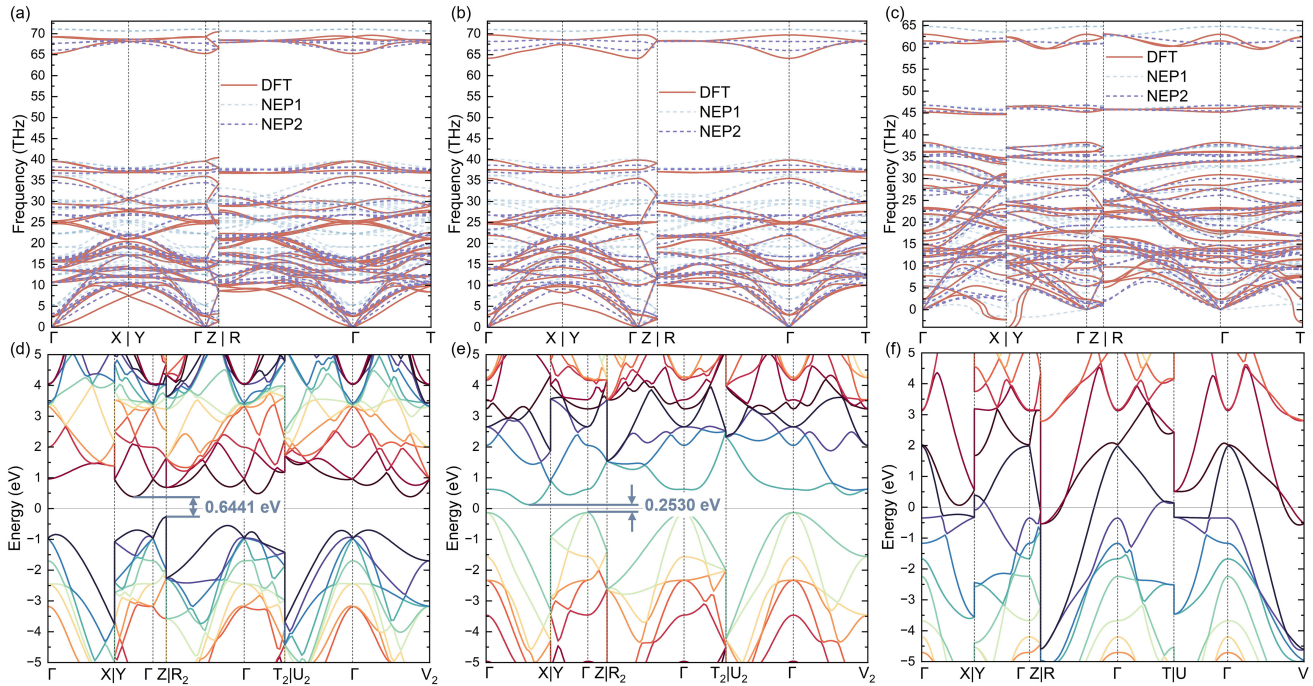


FIG. 7. Comparison of phonon dispersion and electronic band structures for the three standout allotropes. (a)–(c) Phonon spectra for yne-diamond C_{12} , yne-hex-diamond C_8 , and the sp - sp^2 - sp^3 hybridized C_{12} . The plots compare predictions from the initial universal potential (NEP1, dashed light blue lines) and the refined potential (NEP2, dashed purple lines) against ground-truth DFT data (solid red lines), highlighting improvements from active learning iterations. (d)–(f) Corresponding electronic band structures for the same three phases.

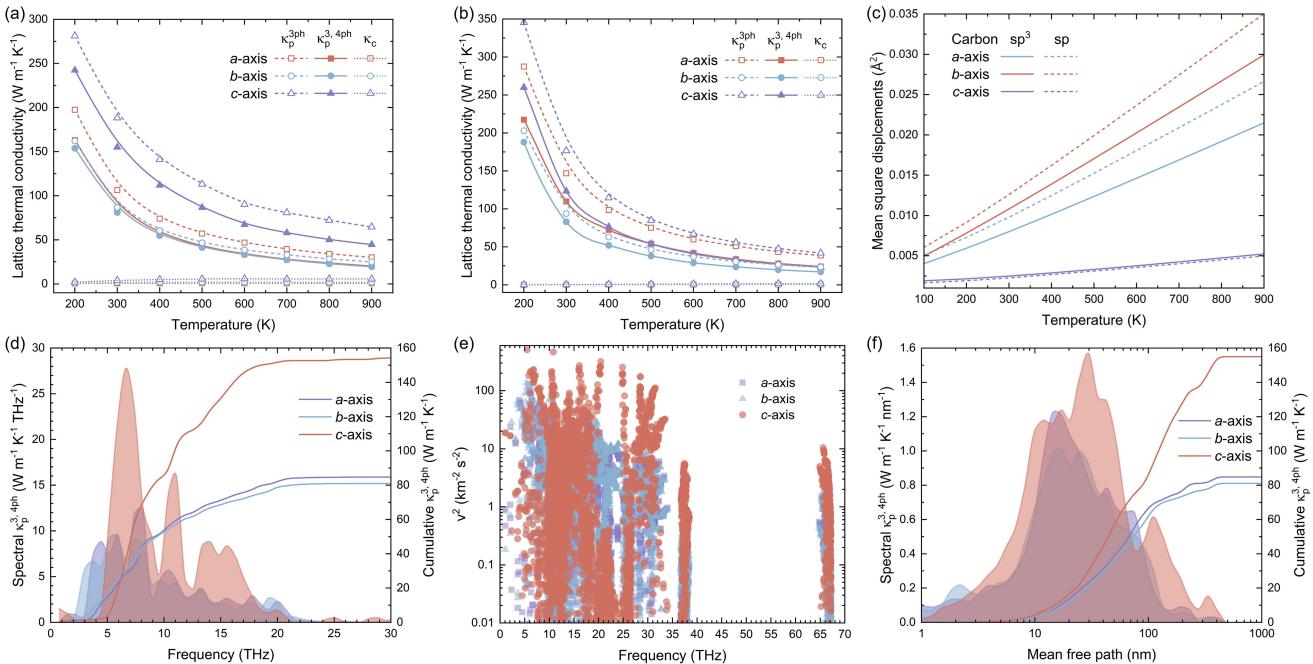


FIG. 8. Microscopic analysis of thermal transport mechanisms. (a, b) Temperature-dependent lattice thermal conductivity (κ_L) for yne-diamond C_{12} and yne-hex-diamond C_8 , decomposed into particle-like (κ_p) and wave-like (κ_c) contributions. (c) Directional mean-square displacement (MSD) of yne-diamond C_{12} . (d)–(f) Spectral analysis for yne-diamond C_{12} at 300 K, considering both three-phonon (3ph) and four-phonon (4ph) scattering: (d) spectral and cumulative κ_L vs. frequency; (e) phonon group velocity; and (f) spectral and cumulative κ_L as a function of the mean free path.

anisms in these newly discovered allotropes, we performed a detailed analysis of their κ_L . Fig. 8 presents the temperature-dependent thermal properties for yne-diamond C_{12} and yne-hex-diamond C_8 . Specifically, Figs. 8(a, b) display the calculated κ_L along the principal crystallographic axes from 200 to 900 K. Utilizing the Boltzmann Transport framework, we decompose κ_L into particle-like propagation (κ_p) [43, 44] and wave-like coherence (κ_c) contributions [45]. The results indicate that κ_L is overwhelmingly dominated by κ_p , while κ_c which is raised from complex inter-band interference remains negligible across the entire temperature range. This dominance confirms that, despite the complex hybridization, heat transport is governed by well-defined phonon wave packets consistent with a crystalline phonon gas model. Furthermore, we assessed the impact of higher-order anharmonicity by comparing results from three-phonon scattering only (κ_p^{3ph}) against those including four-phonon processes ($\kappa_p^{3,4ph}$) [46, 47]. The overlapping curves suggest that four-phonon scattering plays a minor role along the stiff a - and b -axes. However, along the c -axis, higher-order anharmonicity becomes significant, leading to a noticeable reduction in thermal conductivity for both materials [48–53]. As shown in Fig. S6(b), increasing ngrid by 1 from its current value ($8 \times 5 \times 3$ for 3, 4ph processes and $9 \times 6 \times 3$ for 3ph processes in yne-diamond C_{12}) still yields a nearly 10% rise in certain directions, while the current calculations are approaching the limits of existing computational hardware and tools. We look forward to more accurate converged results in the future. Currently, the high-order anharmonicity and BTE calculations of unit cells with a large number of atoms remain an open question.

Both allotropes exhibit strong thermal anisotropy (Figs. 8(a, b)). To identify the atomistic drivers, we analyzed the mean square displacement (MSD) in C_{12} (Fig. 8(c)). The results show that atomic vibrations along the a and b axes significantly exceed those along the c -axis. This finding aligns with the transport data, confirming that the rigid c -axis supports superior heat conduction. Species-resolved MSD analysis further highlights that the sp -hybridized acetylenic linkers possess much larger vibrational amplitudes than the sp^3 atoms. These large-amplitude vibrations of the sp chains in the $a - b$ plane enhance phonon scattering, thereby lowering in-plane κ_L . In contrast, the rigid sp^3 backbone along the c -axis minimizes atomic displacement, ensuring high axial thermal transport.

We further elucidated the heat carrier spectrum by analyzing yne-diamond C_{12} (Fig. 8(d-f)). As shown in Fig. 8(d), heat transport is dominated by acoustic and low-frequency optical phonons (< 15 THz). These modes exhibit distinct spectral peaks corresponding to high group velocities, as confirmed by the v^2 distribution in Fig. 8(e). Crucially, the cumulative thermal conductivity resolved by mean free path (MFP) in Fig. 8(f) reveals

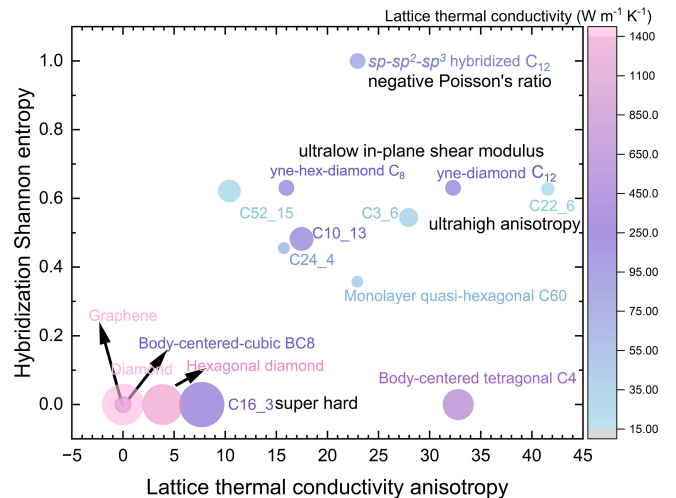


FIG. 9. Multi-dimensional property landscape of discovered carbon allotropes versus established phases (Eq. (1) and (2)). The horizontal axis represents lattice thermal conductivity anisotropy (quantified by RRMSE), while the vertical axis denotes structural complexity measured by the Shannon entropy of hybridization ratios ($sp/sp^2/sp^3$). The data points are color-coded by the average room-temperature lattice thermal conductivity (κ_L), with marker sizes proportional to mass density.

that the primary heat carriers possess MFPs between 10 nm and 100 nm. This finding implies that nanostructuring or grain boundary engineering targeting this length scale would be an effective strategy for tuning the thermal properties of these allotropes. Collectively, our results establish yne-diamond C_{12} as a thermodynamically stable phase with pronounced thermal anisotropy. This transport characteristic originates from the structural contrast between the rigid sp^3 backbone and the soft sp linkers, which act as phonon scattering centers.

To contextualize our findings, Fig. 9 positions the discovered allotropes relative to established carbon phases in a multi-dimensional property landscape. This mapping underscores the ability of the AI workflow to access distinct structural topologies and physical extremes. The horizontal axis represents κ_L anisotropy, quantified by the Relative Root Mean Square Error (RRMSE),

$$\text{RRMSE} = \frac{\sqrt{\frac{1}{3} \sum_{i \in \{a,b,c\}} (\kappa_i - \bar{\kappa})^2}}{\bar{\kappa}} \quad (1)$$

where κ_i and $\bar{\kappa}$ represent the lattice thermal conductivity along the three principal crystallographic axes and average thermal conductivity. The vertical axis measures the structural complexity via the hybridization Shannon entropy (H_{hyb}), calculated based on the proportions of carbon atoms in different hybridization states [54],

$$H_{hyb} = -\left(\sum_{j \in \{sp, sp^2, sp^3\}} p_j \ln p_j \right) / \ln 3 \quad (2)$$

where p_j is the fraction of atoms with hybridization j and $\ln 3$ is the normalization processing. Additionally, the color scale reflects the magnitude of $\bar{\kappa}$, and the size of each data point is proportional to the mass density of the carbon material. Our analysis of structural complexity shown in Fig. 9 reveals a compelling theoretical parallel in the recent work [55], who proposed that heat transport in coordination-disordered solids is fundamentally governed by the bond-network entropy. Despite the rigidity of its sp^3 components, the global lattice thermal conductivity is intrinsically limited by this structural disorder, validating the role of hybridization entropy as a key descriptor for predictive thermal design.

The mapping reveals that unlike diamond and graphene, which reside in low-entropy regions, our generative candidates occupy the high-entropy, high-complexity domain. This complexity enables access to exotic physical properties. A prime example is the sp - sp^2 - sp^3 hybrid C_{12} , which possesses the highest Shannon entropy and displays anomalous auxeticity. The coexistence of this mechanical anomaly with the metallic nature shown in Fig. 7 highlights the capacity of mixed-hybridization networks to realize multifunctional materials inaccessible via conventional heuristic searches.

Moreover, yne-diamond C_{12} and yne-hex-diamond C_8 display ultralow in-plane shear moduli combined with high axial thermal conductivity, positioning them as ideal candidates for flexible thermal interface materials [56]. The versatility of our approach is further exemplified by C22.6, which exhibits giant thermal anisotropy, and C16.3, which resides in the high-density superhard regime. We have thus successfully accessed diverse property domains in carbon materials, including auxetic conductors, superhard insulators, and anisotropic heat spreaders. Ultimately, this work validates the transformative potential of integrating Large Language Models (LLMs) with Machine Learning Potentials to accelerate the inverse design of next-generation functional materials.

As shown in Fig. S4, the cohesive energy of our structures fall near the range of experimentally synthesized metastable carbon allotropes (such as Fullerenes). This energetic proximity suggests they are thermodynamically accessible. More specifically, the cohesive energies of the high-density phases (e.g., C16.3, C24.4) are approximately 7.3-7.6 eV/atom, which is comparable to that of the experimentally synthesized Fullerene (C_{60} , around 7.6 eV/atom) and significantly higher than amorphous carbons. This places them well within the energetic window of synthesizable metastable phases. On the other hand, the mixed-hybridization phases (yne-diamond C_{12} , yne-hex-diamond C_8 , and sp - sp^2 - sp^3 hybridized C_{12}) exhibit cohesive energies around 7.0 eV/atom. While lower than diamond (around 8.0 eV/atom), this reduction is intrinsic to the incorporation of high-energy acetylenic ($-C \equiv C-$) linkages. Their energetic stability relative

to carbyne and graphdiyne. The substantial cohesive energy indicates robust bonding networks resistant to thermal decomposition. We propose that the yne-phases could be realized via bottom-up organic synthesis similar to graphdiyne chemistry [26, 57, 58], while the dense superhard phases (C16.3) are likely accessible via high-pressure confinement of precursors [59].

In summary, we demonstrate a robust AI-driven workflow for accelerating carbon allotrope discovery. By coupling the generative power of Large Language Models with the speed and accuracy of Machine Learning Potentials, this approach circumvents the efficiency bottlenecks of conventional heuristic searches. Central to this success is our dual-loop active learning strategy, which guarantees high model fidelity across broad hybridization and stress regimes, enabling reliable assessments of dynamical stability and thermal transport. Applying this pipeline unlocked carbon phases with unique bonding topologies and functionalities. Notably, yne-diamond C_{12} and yne-hex-diamond C_8 offer high axial thermal conductivity paired with mechanical compliance, targeting flexible electronic applications. Additionally, the identification of the metallic, auxetic sp - sp^2 - sp^3 hybrid C_{12} underscores the method’s ability to access “hidden” regions of the phase diagram. As illustrated in Fig. 9, our analysis links structural complexity directly to exotic performance. Beyond specific material candidates, this study validates a scalable, AI-driven framework for the inverse design of next-generation functional materials.

SUPPLEMENTARY MATERIAL

The Supplementary Material contains unstable carbon structures generated by the LLM with corresponding phonon spectra (Figure S1), and the calculated structural, thermal, and mechanical properties of common and designed novel carbon materials (Table S1). It presents the cumulative and spectral lattice thermal conductivity, weighted phase space, and phonon scattering rates of yne-diamond C_{12} at 300 K (Figure S2), the lattice thermal conductivity versus pressure for diamond at 300 K (Figure S3), and the cohesive energy of common carbon materials compared with designed novel carbon materials (Figure S4, Table S2). Additionally, the variation of stress with triaxial equal strain for diamond and graphite (Figure S5), convergence tests of supercell size and ngrid for lattice thermal conductivity calculations (Figure S6), and the renormalized phonon dispersion curves of yne-diamond C_{12} , yne-hex-diamond C_8 , and sp - sp^2 - sp^3 hybridized C_{12} as a function of temperature (Figure S7) are provided. Detailed computational methods regarding structural optimization, data generation, machine learning potential training, and property calculations, along with the optimized crystal structures (POSCAR) for the discussed carbon allotropes are available.

ACKNOWLEDGEMENTS

We acknowledge the support from the National Natural Science Foundation of China (No.52250191). We also acknowledge the support by HPC Platform, Xi'an Jiaotong University. The data that support the findings of this study are available from the corresponding authors upon reasonable request.

AUTHOR DECLARATIONS

Conflict of interest

The authors have no conflicts to disclose.

† zhibin.gao@xjtu.edu.cn

- [1] R.A. Andrievski, "Superhard materials based on nanostructured high-melting point compounds: achievements and perspectives," *Int. J. Refract. Met. Hard Mat.* **19**, 447–452 (2001).
- [2] Sumio Iijima, "Helical microtubules of graphitic carbon," *Nature* **354**, 56–58 (1991).
- [3] Sumio Iijima and Toshinari Ichihashi, "Single-shell carbon nanotubes of 1-nm diameter," *Nature* **363**, 603–605 (1993).
- [4] D. S. Bethune, C. H. Kiang, M. S. de Vries, G. Gorman, R. Savoy, J. Vazquez, and R. Beyers, "Cobalt-catalysed growth of carbon nanotubes with single-atomic-layer walls," *Nature* **363**, 605–607 (1993).
- [5] Alexander A. Balandin, Suchismita Ghosh, Wenzhong Bao, Irene Calizo, Desalegne Teweldebrhan, Feng Miao, and Chun Ning Lau, "Superior thermal conductivity of single-layer graphene," *Nano Lett.* **8**, 902–907 (2008).
- [6] Artem R. Oganov and Colin W. Glass, "Crystal structure prediction using ab initio evolutionary techniques: Principles and applications," *J. Chem. Phys.* **124**, 244704 (2006).
- [7] Yanchao Wang, Jian Lv, Li Zhu, and Yanming Ma, "Crystal structure prediction via particle-swarm optimization," *Phys. Rev. B* **82**, 094116 (2010).
- [8] Tian Xie and Jeffrey C. Grossman, "Crystal graph convolutional neural networks for an accurate and interpretable prediction of material properties," *Phys. Rev. Lett.* **120**, 145301 (2018).
- [9] Xiaoshan Luo, Zhenyu Wang, Pengyue Gao, Jian Lv, Yanchao Wang, Changfeng Chen, and Yanming Ma, "Deep learning generative model for crystal structure prediction," *npj Comput. Mater.* **10**, 254 (2024).
- [10] Luis M Antunes, Keith T Butler, and Ricardo Grau-Crespo, "Crystal structure generation with autoregressive large language modeling," *Nat. Commun.* **15**, 10570 (2024).
- [11] Zhilong Song, Linfeng Fan, Shuaihua Lu, Chongyi Ling, Qionghua Zhou, and Jinlan Wang, "Inverse design of promising electrocatalysts for CO₂ reduction via generative models and bird swarm algorithm," *Nat. Commun.* **16**, 1053 (2025).
- [12] Amil Merchant, Simon Batzner, Samuel S. Schoenholz, Muratahan Aykol, Gwooon Cheon, and Ekin Dogus Cubuk, "Scaling deep learning for materials discovery," *Nature* **624**, 80–85 (2023).
- [13] Han Yang, Chenxi Hu, Yichi Zhou, Xixian Liu, Yu Shi, Jielan Li, Guanzhi Li, Zekun Chen, Shuizhou Chen, Claudio Zeni, Matthew Horton, Robert Pinsler, Andrew Fowler, Daniel Zügner, Tian Xie, Jake Smith, Lixin Sun, Qian Wang, Lingyu Kong, Chang Liu, Hongxia Hao, and Ziheng Lu, "Mattersim: A deep learning atomistic model across elements, temperatures and pressures," *arXiv:2405.04967* (2024).
- [14] Yujie Liu, Xiaoying Wang, Yuzhou Hao, Xuejie Li, Jun Sun, Turab Lookman, Xiangdong Ding, and Zhibin Gao, "Pink: physical-informed machine learning for lattice thermal conductivity," *J. Mater. Inform.* **5**, 12 (2025).
- [15] Atsushi Togo and Isao Tanaka, "First principles phonon calculations in materials science," *Scr. Mater.* **108**, 1–5 (2015).
- [16] Ke Xu, Hekai Bu, Shuning Pan, Eric Lindgren, Yongchao Wu, Yong Wang, Jiahui Liu, Keke Song, Bin Xu, Yifan Li, Tobias Hainer, Lucas Svensson, Julia Wiktor, Rui Zhao, Hongfu Huang, Cheng Qian, Shuo Zhang, Zezhu Zeng, Bohan Zhang, Benrui Tang, Yang Xiao, Zihan Yan, Jiuyang Shi, Zhixin Liang, Junjie Wang, Ting Liang, Shuo Cao, Yanzhou Wang, Penghua Ying, Nan Xu, Chengbing Chen, Yuwen Zhang, Zherui Chen, Xin Wu, Wenwu Jiang, Esme Berger, Yanlong Li, Shunda Chen, Alexander J. Gabourie, Haikuan Dong, Shiyun Xiong, Ning Wei, Yue Chen, Jianbin Xu, Feng Ding, Zhimei Sun, Tapio Ala-Nissila, Ari Harju, Jincheng Zheng, Pengfei Guan, Paul Erhart, Jian Sun, Wengen Ouyang, Yanjing Su, and Zheyong Fan, "GPUMD 4.0: A high-performance molecular dynamics package for versatile materials simulations with machine-learned potentials," *Mat. Gen. Eng. Adv.* **3**, e70028 (2025).
- [17] Zheyong Fan, Yanzhou Wang, Penghua Ying, Keke Song, Junjie Wang, Yong Wang, Zezhu Zeng, Ke Xu, Eric Lindgren, J. Magnus Rahm, Alexander J. Gabourie, Jiahui Liu, Haikuan Dong, Jianyang Wu, Yue Chen, Zheng Zhong, Jian Sun, Paul Erhart, Yanjing Su, and Tapio Ala-Nissila, "GPUMD: A package for constructing accurate machine-learned potentials and performing highly efficient atomistic simulations," *J. Chem. Phys.* **157**, 114801 (2022).
- [18] A. P. Thompson, H. M. Aktulga, R. Berger, D. S. Bolintineanu, W. M. Brown, P. S. Crozier, P. J. in 't Veld, A. Kohlmeyer, S. G. Moore, T. D. Nguyen, R. Shan, M. J. Stevens, J. Tranchida, C. Trott, and S. J. Plimpton, "LAMMPS - a flexible simulation tool for particle-based materials modeling at the atomic, meso, and continuum scales," *Comp. Phys. Comm.* **271**, 108171 (2022).
- [19] Xiaoying Wang, Zhibin Gao, Guimei Zhu, Jie Ren, Lei Hu, Jun Sun, Xiangdong Ding, Yi Xia, and Baowen Li, "Role of high-order anharmonicity and off-diagonal terms in thermal conductivity: A case study of multiphase CsPbBr₃," *Phys. Rev. B* **107**, 214308 (2023).
- [20] Samir F. Matar and Vladimir L. Solozhenko, "Novel Superhard Tetragonal Hybrid sp^3/sp^2 Carbon Allotropes C_x (x = 5, 6, 7): Crystal Chemistry and *Ab Initio* Studies," *C* **10**, 64 (2024).
- [21] Samir F. Matar, "ene-C₇ (sp^3-sp^2) and yne-C₈ (sp^3-sp^1): Novel ultra-hard trigonal hybrid diamonds from crystal engineering and first principles," *Chin. J. Phys.* **85**, 592–

- 599 (2023).
- [22] Meng Hu, Quan Huang, Zhisheng Zhao, Bo Xu, Dongli Yu, and Julong He, “Superhard and high-strength yne-diamond semimetals,” *Diam. Relat. Mat.* **46**, 15–20 (2014).
- [23] Wei Zhang, Changchun Chai, Qingyang Fan, Yanxing Song, and Yintang Yang, “A novel two-dimensional sp^2 - sp^3 hybridized carbon nanostructure with a negative in-plane Poisson ratio and high electron mobility,” *Comput. Mater. Sci.* **185**, 109904 (2020).
- [24] Alexander J. Gabourie, Zheyong Fan, Tapio Ala-Nissila, and Eric Pop, “Spectral decomposition of thermal conductivity: Comparing velocity decomposition methods in homogeneous molecular dynamics simulations,” *Phys. Rev. B* **103**, 205421 (2021).
- [25] Chengbing Chen, Yutong Li, Rui Zhao, Zhoulin Liu, Zheyong Fan, Gang Tang, and Zhiyong Wang, “Neptrain and neptrainkit: Automated active learning and visualization toolkit for neuroevolution potentials,” *Comput. Phys. Commun.* **317**, 109859 (2025).
- [26] Guoxing Li, Yuliang Li, Huibiao Liu, Yanbing Guo, Yongjun Li, and Daoben Zhu, “Architecture of graphdiyne nanoscale films,” *Chem. Commun.* **46**, 3256–3258 (2010).
- [27] Mengqiu Long, Ling Tang, Dong Wang, Yuliang Li, and Zhigang Shuai, “Electronic structure and carrier mobility in graphdiyne sheet and nanoribbons: Theoretical predictions,” *ACS Nano* **5**, 2593–2600 (2011).
- [28] Jian Zhang, Zhuo Zhao, Miao Jiang, Yuan Cheng, and Gang Zhang, “Thermal properties of hexagonal diamond: Machine learning potential and molecular dynamics study,” *Phys. Rev. Mater.* **9**, 094603 (2025).
- [29] Liuxiang Yang, Kah Chun Lau, Zhidan Zeng, Dongzhou Zhang, Hu Tang, Bingmin Yan, Guoliang Niu, Huiyang Gou, Yanping Yang, Wenge Yang, Duan Luo, and Hokuang Mao, “Synthesis of bulk hexagonal diamond,” *Nature* **644**, 370–375 (2025).
- [30] Yanqing Ge, Shaofeng Huang, Zhehao Yuan, and Wei Zhang, “Crystalline porous frameworks via hierarchical dynamic covalent assembly,” *Acc. Chem. Res.* **58**, 2970–2984 (2025).
- [31] Wenxia Zhang, Baolu Fan, Yumeng Zhang, and Jiyang Fan, “Hydrothermal synthesis of well crystallized C_8 and diamond nanocrystals and pH-controlled C_8 diamond phase transition,” *CrystEngComm* **19**, 1248–1252 (2017).
- [32] P. Liu, H. Cui, and G. W. Yang, “Synthesis of body-centered cubic carbon nanocrystals,” *Cryst. Growth Des.* **8**, 581–586 (2008).
- [33] Roy L. Johnston and Roald Hoffmann, “Superdense carbon, C_8 : supercubane or analog of γ -Si?” *J. Am. Chem. Soc.* **111**, 810–819 (1989).
- [34] Haikuan Dong, Chenyang Cao, Penghua Ying, Zheyong Fan, Ping Qian, and Yanjing Su, “Anisotropic and high thermal conductivity in monolayer quasi-hexagonal fullerene: A comparative study against bulk phase fullerene,” *International Journal of Heat and Mass Transfer* **206**, 123943 (2023).
- [35] Bo Peng and Michele Pizzochero, “Monolayer C_{60} networks: a first-principles perspective,” *Chem. Commun.* **61**, 10287–10302 (2025).
- [36] Bo Peng, “Monolayer fullerene networks as photocatalysts for overall water splitting,” *J. Am. Chem. Soc.* **144**, 19921–19931 (2022).
- [37] Lingxiang Hou, Xueping Cui, Bo Guan, Shaozhi Wang, Ruian Li, Yunqi Liu, Daoben Zhu, and Jian Zheng, “Synthesis of a monolayer fullerene network,” *Nature* **606**, 507–510 (2022).
- [38] Koichiro Umemoto, Renata M. Wentzcovitch, Susumu Saito, and Takashi Miyake, “Body-Centered Tetragonal C_4 : A Viable sp^3 Carbon Allotrope,” *Phys. Rev. Lett.* **104**, 125504 (2010).
- [39] Yang Li, “Body-centered tetragonal C_4 : A carbon allotrope with real topology and second-order bulk-boundary correspondence,” *E Low dimens. Syst. Nanostruct.* **165**, 116070 (2025).
- [40] Xing-Qiu Chen, Haiyang Niu, Dianzhong Li, and Yiyi Li, “Modeling hardness of polycrystalline materials and bulk metallic glasses,” *Intermetallics* **19**, 1275–1281 (2011).
- [41] Faming Gao, Julong He, Erdong Wu, Shimin Liu, Dongli Yu, Dongchun Li, Siyuan Zhang, and Yongjun Tian, “Hardness of covalent crystals,” *Phys. Rev. Lett.* **91**, 015502 (2003).
- [42] Zhibin Gao, Xiao Dong, Nianbei Li, and Jie Ren, “Novel two-dimensional silicon dioxide with in-plane negative poisson’s ratio,” *Nano Letters* **17**, 772–777 (2017).
- [43] Wu Li, Jesús Carrete, Nebil A. Katcho, and Natalio Mingo, “Shengbte: A solver of the boltzmann transport equation for phonons,” *Comput. Phys. Commun.* **185**, 1747–1758 (2014).
- [44] Zherui Han, Xiaolong Yang, Wu Li, Tianli Feng, and Xulin Ruan, “Fourphonon: An extension module to shengbte for computing four-phonon scattering rates and thermal conductivity,” *Comput. Phys. Commun.* **270**, 108179 (2022).
- [45] Michele Simoncelli, Nicola Marzari, and Francesco Mauri, “Unified theory of thermal transport in crystals and glasses,” *Nat. Phys.* **15**, 809–813 (2019).
- [46] Minxuan Feng, Xiaoying Wang, Guimei Zhu, Cheng He, Jun Sun, Xiangdong Ding, Junichiro Shiomi, Yi Xia, Baowen Li, and Zhibin Gao, “The relation between the atomic mass ratio and quartic anharmonicity in alkali metal hydrides,” *Mater. Today Phys.* **44**, 101423 (2024).
- [47] Yi Xia, Vinay I. Hegde, Koushik Pal, Xia Hua, Dale Gaines, Shane Patel, Jiangang He, Muratahan Aykol, and Chris Wolverton, “High-throughput study of lattice thermal conductivity in binary rocksalt and zinc blende compounds including higher-order anharmonicity,” *Phys. Rev. X* **10**, 041029 (2020).
- [48] Yuzhou Hao, Yuting Zuo, Jiongzhi Zheng, Wenjie Hou, Hong Gu, Xiaoying Wang, Xuejie Li, Jun Sun, Xiangdong Ding, and Zhibin Gao, “Machine learning for predicting ultralow thermal conductivity and high zt in complex thermoelectric materials,” *ACS Appl. Mater. Interfaces* **16**, 47866–47878 (2024).
- [49] Yang Wang, Zhibin Gao, Xiaoying Wang, Jinping Sun, Minxuan Feng, Yuzhou Hao, Xuejie Li, Yinchang Zhao, and Xiangdong Ding, “Anomalous thermal conductivity in 2D silica nanocages of immobilizing noble gas atom,” *Appl. Phys. Lett.* **124**, 122205 (2024).
- [50] Xiaoying Wang, Mengyang Li, Minxuan Feng, Xuejie Li, Yuzhou Hao, Wen Shi, Jiangang He, Xiangdong Ding, and Zhibin Gao, “Bonding hierarchy and coordination interaction leading to high thermoelectricity in wide bandgap $TlAgL_2$,” *Phys. Rev. Mater.* **8**, 094601 (2024).
- [51] Xiaoying Wang, Minxuan Feng, Yi Xia, Jun Sun, Xiangdong Ding, Baowen Li, and Zhibin Gao, “Revisiting lattice thermal conductivity of CsCl: The crucial role of

- quartic anharmonicity,” *Appl. Phys. Lett.* **124**, 172201 (2024).
- [52] Minxuan Feng, Xiaoying Wang, Guimei Zhu, Cheng He, Jun Sun, Xiangdong Ding, Junichiro Shiomi, Yi Xia, Baowen Li, and Zhibin Gao, “The relation between the atomic mass ratio and quartic anharmonicity in alkali metal hydrides,” *Mater. Today Phys.* **44**, 101423 (2024).
- [53] Yuzhou Hao, Junwei Che, Xiaoying Wang, Xuejie Li, Turab Lookman, Jun Sun, Xiangdong Ding, and Zhibin Gao, “Copper delocalization leads to ultralow thermal conductivity in chalcogenide CuBiSeCl_2 ,” *Phys. Rev. B* **111**, 195207 (2025).
- [54] C. E. Shannon, “A mathematical theory of communication,” *Bell Syst. Tech. J* **27**, 379–423 (1948).
- [55] Kamil Iwanowski, Gábor Csányi, and Michele Simoncelli, “Bond-network entropy governs heat transport in coordination-disordered solids,” *Phys. Rev. X* **15**, 041041 (2025).
- [56] Jie Chen, Xiangfan Xu, Jun Zhou, and Baowen Li, “Interfacial thermal resistance: Past, present, and future,” *Rev. Mod. Phys.* **94**, 025002 (2022).
- [57] Ryota Matsuoka, Ryota Sakamoto, Ken Hoshiko, Sono Sasaki, Hiroyasu Masunaga, Kosuke Nagashio, and Hiroshi Nishihara, “Crystalline graphdiyne nanosheets produced at a gas/liquid or liquid/liquid interface,” *Journal of the American Chemical Society* **139**, 3145–3152 (2017).
- [58] Jinying Zhang, Rui Wang, Xi Zhu, Aifei Pan, Chenxiao Han, Xin Li, Dan Zhao, Chuansheng Ma, Wenjun Wang, Haibin Su, and Chunming Niu, “Pseudo-topotactic conversion of carbon nanotubes to t-carbon nanowires under picosecond laser irradiation in methanol,” *Nat. Commun.* **8**, 683 (2017).
- [59] Meng Hu, Julong He, Zhisheng Zhao, Timothy A. Strobel, Wentao Hu, Dongli Yu, Hao Sun, Lingyu Liu, Ziheng Li, Mengdong Ma, Yoshio Kono, Jinfu Shu, Ho kwang Mao, Yingwei Fei, Guoyin Shen, Yanbin Wang, Stephen J. Juhl, Jian Yu Huang, Zhongyuan Liu, Bo Xu, and Yongjun Tian, “Compressed glassy carbon: An ultrastrong and elastic interpenetrating graphene network,” *Sci. Adv.* **3**, e1603213 (2017).